An Improved Virtual Inertia Algorithm of Virtual Synchronous Generator

Haizhen Xu, Changzhou Yu, Chun Liu, Qinglong Wang, and Xing Zhang

***Abstract*—Virtual synchronous generator (VSG) simulates the first-order motion equation of a synchronous generator (SG) with the algorithm. VSG can improve the system voltage and frequency support capabilities of a microgrid or a weak grid. It is now widely applied at a high penetration level of distributed generation (DG) systems. However, because there is a contradiction between active power steady-state deviation of VSG and dynamic impact regulation, the VSG running in grid-connected mode with existing strategies cannot meet the steady and dynamic control requirements. Thus, an improved virtual inertial control strategy of VSG is proposed in this paper. The active power impact is reduced effectively under the circumstance of damping coefficient D_ω equal to 0 and a large inertia, thus the dynamic characteristic of active power is improved and its steady-state characteristic is maintained. Firstly, based on the analysis of the damping coefficient effect on the system dynamic process, two forms of improved virtual inertia algorithms are put forward by cascading a differential link into different positions of the first-order virtual inertia forward channel. Then, by comparing the characteristics of the system with the two improved algorithms, the improved virtual inertial strategy based on differential compensation is proven to be better, and the design of its parameters is analyzed. Finally, simulation and experimental results verify the effectiveness of the proposed algorithm.**

***Index Terms*—Virtual synchronous generator (VSG), virtual inertia, microgrid, distributed generation (DG).**

I. Introduction

With the massive consumption of non-renewable energy and increasingly severe environmental pollution, distributed generation (DG) such as photovoltaic (PV) and wind power has become the focus of attention, and is developing rapidly and applied widely [1]-[5].

A grid-connected PV inverter adopts the maximum power point tracking (MPPT) algorithm and the phase locked loop (PLL) algorithm to ensure the maximum output power to the grid [6]. However, the PV inverter is not able to provide frequency support for the grid because their frequencies are decoupling controlled. As the penetration of PV sources increases, the grid frequency fluctuation increases and the system stability deteriorates.

To solve this problem, a virtual synchronous generator (VSG) method is proposed [7]-[11]. By configuring energy storage devices in an isolated microgrid or weak grid with high penetration of DG and employing a control algorithm to simulate the torque equation and electrical equation of a synchronous generator (SG), the system inertia can be increased, and the frequency fluctuation is reduced.

The existing literature on VSG describes the simulation of different orders of the SG model, but all have first-order virtual inertia. In terms of frequency regulation, VSG based on first-order virtual inertia can restrain frequency fluctuation. However, its overload capacity is lower than a real SG. A sizeable virtual inertia may enhance the frequency support capability of VSG and cause oscillation of output active power at low frequency or a large overshoot, which results in significant power surge of the energy storage unit and VSG overcurrent protection. In order to reduce power overshoot, the damping coefficient needs to be increased accordingly. But the increase of damping coefficient also leads to an increase of steady-state power deviation of the grid-connected VSG, especially in a weak grid. Therefore, there exist contradictions between output active power steady-state deviation and dynamic impact regulation of VSG with a first-order virtual inertia algorithm in grid-connected mode.

A lot of work has been done to deal with the problem. In [12]-[16], the principle of power oscillation caused by virtual inertia, and the influence of damping coefficient on dynamic and steady-state characteristics of VSG are analyzed. However, the system performance is improved only by compromising choices of parameters, but not by overcoming it fundamentally. In [13], a virtual inertia bang-bang control strategy is presented. The virtual inertia is dynamically changed to the maximum value or the minimum value according to the frequency difference between VSG and the grid as well as the rate of change of VSG frequency. This method reduces the dynamic overshoot of active power while maintaining its steady-state power control accuracy. But it requires a higher tracking speed and frequency accura-

Manuscript received: July 19, 2018; accepted: May 28, 2019. Date of Cross-Check: May 28, 2019. Date of online publication: October 9, 2019.

This work was supported by the Natural Science Foundation of Anhui Province of China (No. 1908085QE208, No. 1808085QE156), and the 2018 Academic Foundation Program for the Major's Talents of Anhui Colleges and Universities (No. GXBJZD40).

H. Xu, C. Yu (corresponding author), C. Liu, and Q. Wang are with the Department of Electronic Information and Electrical Engineering, Hefei University, Hefei, China (e-mail: xhzicy@sina.com; ycz87@163.com; 40367085@qq.com; wangqlong@hfuu.edu.cn).

X. Zhang is with Anhui Provincial Engineering Laboratory of Renewable Energy and Industrial Energy Conservation, Hefei University of Technology, Hefei, China (e-mail: honglf@ustc.edu.cn).

DOI: 10.35833/MPCE.2018.000472

cy, and an improper frequency threshold may lead to the jittering of the virtual inertia value, resulting in VSG frequency and power fluctuations. In [14], [15], an optimal virtual inertia and virtual damping coefficients are calculated in real time according to power optimization algorithm of VSG, which reduces power overshoot. However, grid frequency monitoring and complicated calculation of optimization algorithm in real time are prerequisites, and the steady-state power control precision is not considered.

In summary, the existing approaches are based on the compromise or real-time change of virtual inertia and damping coefficient according to the system state to improve the dynamic characteristics of the system. But the compromise scheme cannot meet the high requirements of the system, and the real-time change of parameters can easily cause system instability. In addition, the effect of parameter changes on steady-state characteristics of the system is not considered.

In this paper, an improved virtual inertial control strategy of VSG is proposed and three objectives have been achieved: ① the contradiction between active power steady-state deviation and dynamic impact of VSG with the existing first-order virtual inertia algorithm is analyzed; ② the damping coefficient $D_\omega = 0$ is set and an improved virtual inertia control strategy is proposed to increase system damping and reduce dynamic power impact while keeping steady-state deviation unchanged. Compared with the existing methods, the proposed strategy does not need to change parameters in real time, thus it has higher stability; ③ simulations and experiments are conducted on a grid-connected VSG with first-order virtual inertia and an improved virtual inertia strategy. Experimental results show that VSG with the first-order virtual inertia strategy reduces the dynamic power impact accompanied by an increase of steady-state power deviation. However, VSG with the improved virtual inertia strategy reduces dynamic power impact when the steady-state power deviation is maintained. In addition, the dynamic power impact generated by differential compensation at Position 1 is the smallest.

This paper is organized as follows. In Section II, the frequency and active power characteristics of the first-order virtual inertial VSG are analyzed, and the contradiction between steady-state and dynamic characteristic of active power is put forward. Section III presents the improved virtual inertial based on differential compensation. Section IV presents simulation and experimental results. Section V is the conclusion.

II. Analysis of First-order Virtual Inertia Characteristics and Its Problem

A. Introduction of VSG Control Strategy

Figure 1 is the main circuit and control structure of VSG. When switch KM is closed, VSG is operated in grid-connected mode. When KM is disconnected, VSG is operated in isolated mode. L_f and r_{Lf} are the filter inductor and the parasitic resistance of VSG, respectively; C_f is the filter capacitor; L_l and r_l are the line impedance, respectively; i_{Lfa}, i_{Lfb}, i_{Lfc} are three-phase currents of the filter inductor; u_{0a}, u_{0b}, u_{0c} are the three-phase output voltages of the VSG; u_{ga}, u_{gb}, u_{gc} are the three-phase voltages of the power grid; P_0 and Q_0 are the output active power and reactive power of VSG, respectively; ω is the angular frequency of reference voltage; and E^* is the rated voltage amplitude.

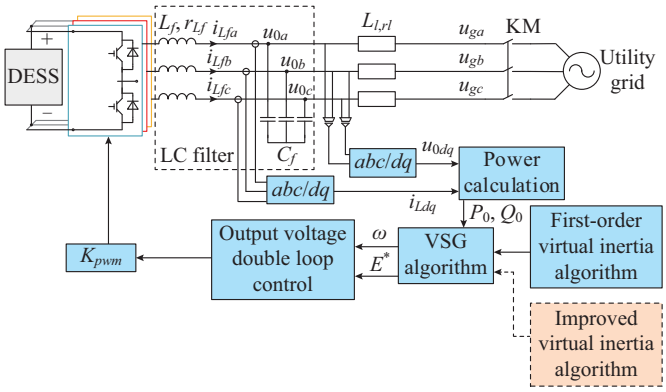

Fig. 1. Main circuit and control structure of VSG.

The VSG algorithm simulates the mechanical torque equation and reactive power droop characteristic of SG, as shown in (1) [17], [18]:

$$\begin{cases} J_\omega \omega_0 \dfrac{\mathrm{d}\omega}{\mathrm{d}t} = P_{ref} + K_\omega\left(\omega_0 - \omega\right) - P_0 - D_\omega \Delta\omega \\ E = E^* - \dfrac{n}{T_f s + 1} Q_0 \end{cases} \tag{1}$$

where J_ω is the virtual inertia; ω_0 is angular frequency; E is amplitude of reference voltage; P_{ref} is reference active power; K_ω is the speed governor coefficient; n is the reactive power droop coefficient; and T_f is the time constant of the first-order low pass filter.

B. Frequency Characteristics of Islanded VSG with First-order Virtual Inertial

According to Fig. 1 and (1), when the first-order virtual inertia VSG is operated in isolated mode, its block diagram of angular frequency closed-loop control is shown in Fig. 2.

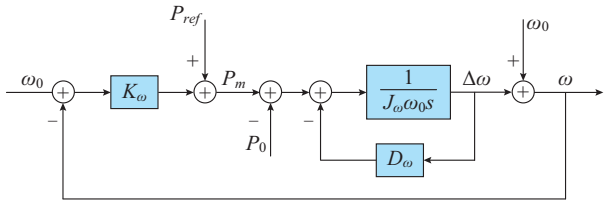

Fig. 2 Angular frequency closed-loop control of VSG.

When the VSG is operated independently with load, its output power P_0 is determined by the active load, and the output voltage angular frequency ω varies with P_0. The transfer function of output active power to angular frequency (P-ω) is:

$$G_{P\text{-}\omega}=\frac{\omega-\omega_0}{P_{ref}-P_0}=\frac{\Delta\omega}{\Delta P}=\frac{1}{J_\omega\omega_0 s+K_\omega+D_\omega} \tag{2}$$

The VSG P-ω transfer function is a first-order inertia link. Its time constant is determined by J_ω, K_ω and D_ω, and the steady-state frequency deviation is determined by K_ω and D_ω. Although the physical meaning of K_ω and D_ω is different, their effect on the steady-state and dynamic characteristics of VSG output active power are the same. Generally, $\Delta\omega_{\max}/\Delta P_{\max}=1/\left(K_\omega+D_\omega\right)=0.01\omega_0/S_{rate}$ [19], and S_{rate} is the VSG rated capacity. Considering that some synchronous motors are without damping windings, and for ease of analysis, $1/K_\omega$ = $0.01\omega_0/S_{rate}$ is taken as a fixed value and $D_\omega \geqslant 0$ as a variable parameter, thus the active power characteristics can be adjusted by changing D_ω.

Figure 3 is the step response curve of $\Delta\omega$ with ΔP_0 = S_{rate}. It can be seen that, the larger the J_ω, the larger the inertia time constant, and the slower the variation of ω in the dynamic process. While the larger the D_ω, the faster the variation of ω in the dynamic process, and the smaller the steady-state frequency deviation. Therefore, J_ω affects the dynamic properties of $\Delta\omega$, while D_ω has an effect on both the dynamic and steady-state properties of $\Delta\omega$.

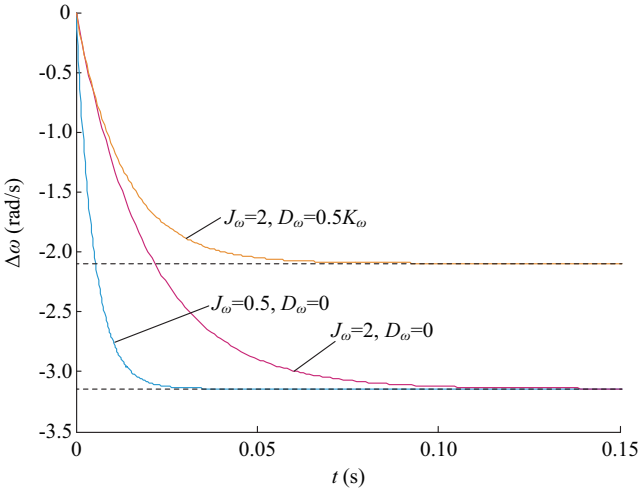

Fig. 3 Step response curve of $\Delta\omega$.

C. Active Power Characteristics of Grid-connected VSG with First-order Virtual Inertial

When the VSG is operated in grid-connected mode, its closed-loop control of output active power is shown in Fig. 4, where K_p = $3U_0U_g/X_l$; U_0 and U_g are VSG output voltage amplitude and the grid voltage amplitude, respectively; and ω_g is the angular frequency of the grid.

According to Fig. 4, the closed-loop transfer function of VSG output active power P_{out} can be obtained:

$$P_0=\frac{K_P}{J_\omega\omega_0 s^2+\left(K_\omega+D_\omega\right)s+K_P}P_{ref}+\frac{K_P\left(J\omega_0 s+K_\omega+D_\omega\right)}{J_\omega\omega_0 s^2+\left(K_\omega+D_\omega\right)s+K_P}\cdot$$
$$\left(\omega_0-\omega_g\right)=G_r(s)P_{ref}+G_f(s)\left(\omega_0-\omega_g\right) \tag{3}$$

where $G_r(s)$ is a second-order expression.

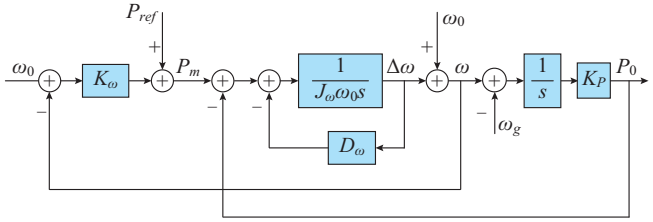

Fig. 4. Closed-loop control of active power of VSG.

If the grid is a utility one with constant frequency and ω_g = ω_0, in steady state, the VSG frequency is clamped by the grid, and thus ω = ω_g. Under this circumstance, the speed governor does not work, and P_0 is to P_{ref}. If the grid is weak or at the end of a large utility grid, its frequency fluctuates slowly, and it can be considered that $\omega_g \neq \omega_0$ in steady state. Thereby, the output active power of VSG consists of two parts: P_{ref} and power deviation $\left(K_\omega+D_\omega\right)\left(\omega_0-\omega_g\right)$ caused by frequency difference. Under the condition that K_ω is fixed, the power deviation increases linearly with D_ω. However, when the VSG operates in grid-connected mode, its output power is required to follow the power command, and a large power deviation may lead to the system deviation from power scheduling. Hence, D_ω should be chosen as small as possible to reduce the steady-state deviation of active power.

The dynamic characteristic of VSG output active power can be analyzed by taking advantage of the system closed-loop small-signal model. According to (3), the closed-loop small signal transfer function of active power can be gained:

$$G_r(s)=\frac{\Delta P_{out}}{\Delta P_{ref}}=\frac{K_P}{J_\omega\omega_0 s^2+\left(K_\omega+D_\omega\right)s+K_P} \tag{4}$$

The damping ratio ξ_{Gr} and natural oscillation frequency ω_{nGr} are [20]:

$$\begin{cases}\xi_{Gr}=\dfrac{K_\omega+D_\omega}{2\sqrt{K_P J_\omega\omega_0}}\\ \omega_{nGr}=\sqrt{\dfrac{K_P}{J_\omega\omega_0}}\end{cases} \tag{5}$$

The system damping ratio is determined by J_ω and D_ω, and the increase of D_ω or the decrease of J_ω can both increase ξ_{Gr} to reduce power impact [21]. Natural oscillation frequency of the system is determined by J_ω, and the increase of J_ω can reduce ω_{nGr}.

In order to ensure good dynamic characteristics and system stability, J_ω and D_ω should meet the following conditions.

1) Damping ratio condition: for a typical second-order system, damping ratio is generally selected as $0.5<\xi<1$ to ensure fast dynamic response and good stability [22]. For the grid-connected VSG system, a large output power overshoot in dynamic process increases the power impact of the energy storage unit and may cause overcurrent of VSG. To avoid excessive power overshoot, ξ_{Gr} is set to satisfy:

$$0.8 \le \xi_{Gr} \le 1 \tag{6}$$

2) Stability margin condition: considering the influence of system parameters and other factors on system stability, an appropriate margin should be retained when selecting parameters. In this paper, the amplitude margin h and phase angular margin γ are set to satisfy:

$$\begin{cases} h = +\infty > 6\,\text{dB} \\ \gamma = \arctan\left(2\xi_{Gr} \left(\dfrac{1}{\sqrt{4\xi_{Gr}^4 + 1} - 2\xi_{Gr}^2} \right)^{1/2} \right) > 60^\circ \end{cases} \tag{7}$$

3) Adjustment time condition: the adjustment time of a second-order system is related to the real-part position of closed-loop poles. The farther the real part is from the imaginary axis, the shorter the adjustment time will be. In addition, system stability is also related to the position of the closed-loop poles. The system is stable under the condition where the closed-loop poles are all located in the left half of the s plane. However, due to parameter change, the poles may move to the right half of the s plane. The closer the closed-loop poles are to the imaginary axis, the smaller the system stability margin will be. Therefore, the distance of closed-loop poles to the imaginary axis can also be used to measure the stability margin of the system.

Considering adjustment time and system stability, closed-loop poles are set to satisfy:

$$Re\left(s_i\right) = -\omega_{nGr}\xi_{Gr} \le -10 \tag{8}$$

where $Re\left(s_i\right)$ is the real part of closed-loop pole.

4) Inner and outer loop decoupling condition: we aim to eliminate the impact of the inner voltage loop on the outer power control loop and ensure the same low-frequency characteristics of VSG as SG. The inner voltage loop response should be fast enough to be equal to a proportional link of 1, which is relative to the outer power control loop [23]. We set the bandwidth of the inner loop to ω_b = 200 × 2π rad/s, and that of the outer power loop should satisfy $\omega_{fb} \le \omega_{ub}/4$, which is:

$$\omega_{fb} = \omega_{nGr}\left[\left(1 - 2\xi_{Gr}^2\right) + \sqrt{\left(1 - 2\xi_{Gr}^2\right)^2 + 1} \right]^{1/2} \le 50 \times 2\pi \tag{9}$$

The curves in Fig. 5 are J_ω and D_ω values which meet system boundary conditions of damping ratio, stability margin, adjustment time, inner and outer loop decoupling. The shadow surrounded by the curves are J_ω and D_ω values that meet the conditions. This is mainly restricted by the damping ratio and adjustment time constraints. In order to improve system inertia, a bigger J_ω is essential, while for the maintenance of system dynamic characteristic, D_ω should increase with J_ω in the shadow range.

D. Contradiction Between Steady-state and Dynamic Characteristic Regulation

In summary, when VSG based on first-order virtual inertia operates in grid-connected mode, J_ω only affects dynamic characteristics of active power, while D_ω affects both dynamic and steady-state characteristics of active power.

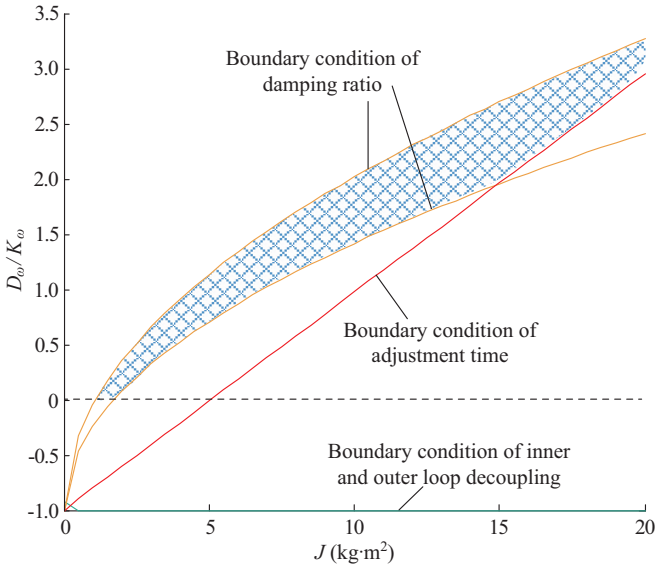

Fig. 5. Values of J_ω and D_ω satisfying dynamic characteristic requirements of grid-connected VSG.

In order to improve the system dynamic characteristics with a large inertia, D_ω should be increased accordingly, but the deviation of steady-state active power is increased at the same time. Therefore, there is a regulation contradiction between steady-state deviation of output active power and dynamic impact of VSG operating in grid-connected mode. In order to solve this problem, $D_\omega = 0$ is set to eliminate the coupling effect of D_ω on steady-state deviation of active power and dynamic impact, thus the deviation of system active power can be maintained. Furthermore, to improve the system dynamic characteristics, a new algorithm is proposed in Section III to replace the regulation effect of D_ω on active power dynamic features, so that the dynamic power impact still meets the system requirement when there is a larger J_ω.

III. Improved Virtual Inertial Control Strategy Based on Differential Compensation

A. Principle of Improved Virtual Inertia Based on Differential Compensation

Suppose the active power reference steps from 0 to P_{ref} at time t_0. The waveforms of output active power of VSG P_{out}, the output voltage and grid voltage difference δ_{out}, the output voltage angular frequency ω_{out} and the change rate of angular frequency dω/dt are shown in Fig. 6. P_{refs}, δ_{outs}, ω_{outs} are the corresponding values when VSG achieves steady state.

In the time period $t_0 - t_1$, $\Delta P_{out} = P_{out} - P_{outs} < 0$, which makes d$\omega$/d$t > 0$, and therefore $\Delta\omega = \omega_{out} - \omega_{outs} > 0$ and it increases gradually. Thus $\Delta\delta = \delta_{out} - \delta_{outs} > 0$, and P_{out} increases. At time t_1, $P_{out} = P_{ref}$ and dω/d$t = 0$. However, because of the large inertia effect, $\Delta\omega$ cannot decrease to 0 immediately, which results in the continuous rise of P_{out} and causes a high power overshoot at the end. At time t_2, P_{out} reaches the maximum value, and $\Delta\omega = 0$. Because the system is convergent, the oscillation amplitude decreases in each oscillation period, and finally the steady state is achieved.

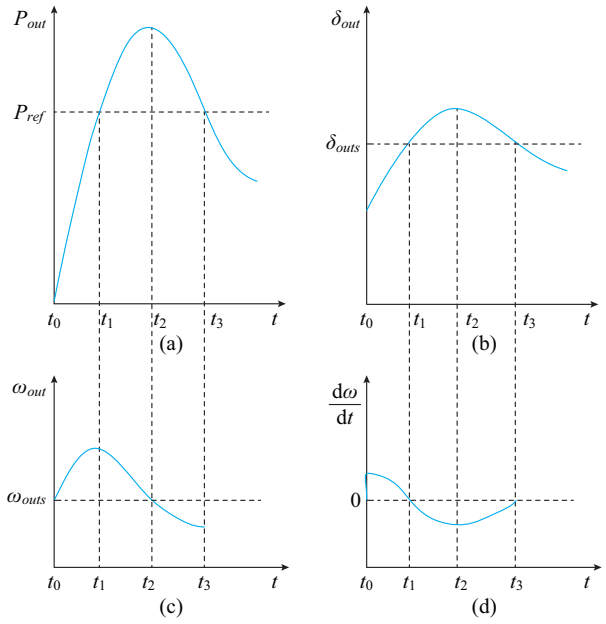

Fig. 6. Waveforms of parameters in dynamic process. (a) P_{out}. (b) δ_{out}. (c) ω_{out}. (d) $d\omega/dt$.

The reason why a large overshoot of output active power is produced is that $\Delta\omega$ cannot quickly approach 0 at time $d\omega/dt = 0$, resulting in continuous increase or decrease of $\Delta\delta$.

In the automatic control principle, a differential link is generally used to correct a signal in advance to increase system damping and speed up system response without affecting the steady-state errors of the system. Therefore, a differential compensation link is added in the forward channel of VSG active power control loop to improve the dynamic characteristic of the system instead of setting a large value of D_ω. The steady-state characteristic of the system is not affected.

According to the block diagram of VSG control, there are two ways for differential compensation link added in the forward channel. One way is adding a derivative of active power difference, which reduces ω value by advance correction of $d\omega/dt$, as shown at Position 1 in Fig. 7. Another way is to superimpose the derivative $d\omega/dt$ directly on ω, as shown at Position 2 in Fig. 7 [24]. In the two ways, K_d is the differential coefficient. The control structure of the grid-connected VSG system based on the improved virtual inertia algorithm can be obtained by replacing the first-order virtual inertia in Fig. 2 with the improved virtual inertia shown in the dotted line.

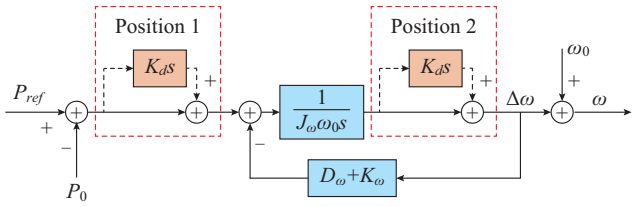

Fig. 7. Two methods of differential compensation link addition.

B. Frequency Characteristics of Islanded Operating VSG with Improved Virtual Inertial Based on Differential Compensation

When VSG operates in islanded mode, and if differential compensation is added at Position 1, the output power-angular frequency (P-ω) transfer function is:

$$G_{P-\omega,d1} = \frac{\omega-\omega_0}{P_{ref}-P_0} = \frac{\Delta\omega}{\Delta P} = \frac{1+K_d s}{J_\omega \omega_0 s + K_\omega + D_\omega} \tag{10}$$

If differential compensation is added at Position 2, the transfer function output power-angular frequency (P-ω) is:

$$G_{P-\omega,d2} = \frac{\omega-\omega_0}{P_{ref}-P_0} = \frac{\Delta\omega}{\Delta P} = \frac{1+K_d s}{\left(J_\omega \omega_0 + K_d K_\omega + K_d D_\omega\right) s + K_\omega + D_\omega} \tag{11}$$

With the differential compensation, the P-ω characteristic is changed from a first-order inertia link to a lead-lag link. In (10), K_d is related to zero and is independent of the pole. If K_d is small, the zero is far away from the imaginary axis and can be ignored. The dynamic characteristics is mainly affected by the pole, and $G_{P\text{-}\omega,d1}$ is approximated as a first-order inertia link. If K_d is large, the zero approaches the origin, and $G_{P\text{-}\omega,d1}$ is equivalent to a differential link. In (11), K_d is related to both zero and pole. If K_d is small, $G_{P\text{-}\omega,d2}$ is approximated as a first-order inertia link; if K_d is large, the zero and the pole form a pair of dipoles, $G_{P\text{-}\omega,d2}$ is approximated as a linear droop link, and the droop coefficient is related to K_ω and D_ω. However, K_d does not change the steady-state operating point of the VSG, and the steady-state frequency deviations of (10) and (11) are still determined by K_ω and D_ω.

Setting J_ω and K_ω as unchanged, in Fig. 8 are P-ω characteristic curves of (10) and (11) with different D_ω, K_d values. It can be seen that $G_{P\text{-}\omega,d1}$ and $G_{P\text{-}\omega,d2}$ are droop links in the early stage of the power step, and are first-order inertia links in the latter stage, so they have both fast response characteristics of droop control and large inertia characteristic of a first-order link. In the case of the same K_d, the inertia of $G_{P\text{-}\omega,d1}$ is smaller than that of $G_{P\text{-}\omega,d2}$. In Fig. 8, $G_{P\text{-}\omega,d1,2}$ denotes $G_{P\text{-}\omega,d1}$ and $G_{P\text{-}\omega,d2}$.

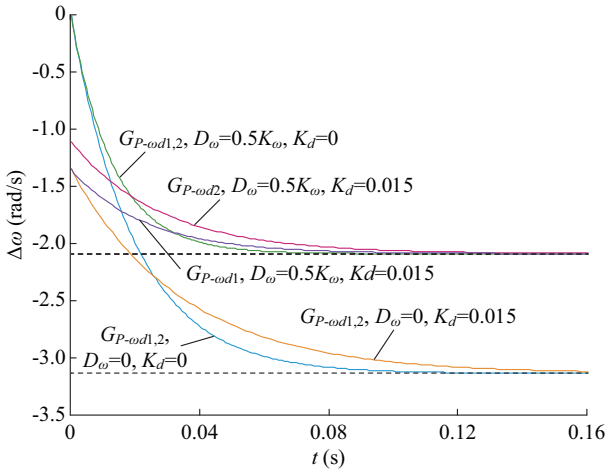

Fig. 8. P-ω curves of VSG with differential compensation link.

C. Active Power Characteristics of Grid-connected VSG with Improved Virtual Inertial Based on Differential Compensation

When VSG operates in grid-connected mode, and if differential compensation is added at Position 1, the closed-loop transfer function of output active power is:

$$P_{0,d1}=\frac{K_P\left(1+K_d s\right)P_{ref}}{J_\omega\omega_0 s^2+\left(K_\omega+D_\omega+K_P K_d\right)s+K_P}+\frac{K_P\left(J_\omega\omega_0 s+K_\omega+D_\omega\right)\left(\omega_0-\omega_g\right)}{J_\omega\omega_0 s^2+\left(K_\omega+D_\omega+K_P K_d\right)s+K_P}=G_{r,d1}(s)P_{ref}+G_{f,d1}(s)\left(\omega_0-\omega_g\right) \tag{12}$$

If differential compensation is added at Position 2, the closed-loop transfer function of output active power is:

$$P_{0,d2}=\frac{K_P\left(1+K_d s\right)P_{ref}}{\left(J_\omega\omega_0+K_d\left(K_\omega+D_\omega\right)\right)s^2+\left(K_\omega+D_\omega+K_P K_d\right)s+K_P}+\frac{\left\{K_P\left[J_\omega\omega_0+K_d\left(K_\omega+D_\omega\right)\right]s+K_\omega+D_\omega\right\}\left(\omega_0-\omega_g\right)}{\left[J_\omega\omega_0+K_d\left(K_\omega+D_\omega\right)\right]s^2+\left(K_\omega+D_\omega+K_P K_d\right)s+K_P}=G_{r,d2}(s)P_{ref}+G_{f,d2}(s)\left(\omega_0-\omega_g\right) \tag{13}$$

According to (12) and (13), the steady-state output active power of VSG with two different differential compensation ways are as follows:

$$\begin{cases}P_{0,d1s}=\lim\limits_{s\to 0}\left(G_{r,d1}(s)P_{ref}+G_{f,d1}(s)(\omega_0-\omega_g)\right)\\ \quad=P_{ref}+(K_\omega+D_\omega)(\omega_0-\omega_g)\\ P_{0,d2s}=\lim\limits_{s\to 0}\left(G_{r,d2}(s)P_{ref}+G_{f,d2}(s)(\omega_0-\omega_g)\right)\\ \quad=P_{ref}+(K_\omega+D_\omega)(\omega_0-\omega_g)\end{cases} \tag{14}$$

As with first-order virtual inertia VSG, when VSG with improved virtual inertial based on differential compensation is operated in grid-connected mode, its steady-state output active power consists of two parts: P_{ref} and $(K_\omega+D_\omega)(\omega_0-\omega_g)$ caused by frequency difference. The power deviation increases linearly with D_ω, and the differential compensation does not affect the steady-state characteristics of the system.

The active power dynamic characteristic of VSG with improved virtual inertial can be analyzed by taking advantage of closed-loop small-signal model of the system. According to (12) and (13), the closed-loop small signal transfer function of active power can be obtained:

$$\begin{cases}G_{r,d1}(s)=\dfrac{\Delta P_{0,d1}}{\Delta P_{ref}}=\dfrac{K_P\left(1+K_d s\right)}{J_\omega\omega_0 s^2+\left(K_\omega+D_\omega+K_P K_d\right)s+K_P}\\ G_{r,d2}(s)=\dfrac{\Delta P_{0,d2}}{\Delta P_{ref}}=\dfrac{K_P\left(1+K_d s\right)}{\left[J_\omega\omega_0+K_d\left(K_\omega+D_\omega\right)\right]s^2+\left(K_\omega+D_\omega+K_P K_d\right)s+K_P}\end{cases} \tag{15}$$

$G_{r,d1}(s)$ and $G_{r,d2}(s)$ are both second-order systems with one same zero point which is determined by K_d. Their damping ratios $\xi_{G_{r,d1}}$, $\xi_{G_{r,d2}}$ and natural oscillation frequencies $\omega_{nG_{r,d1}}$, $\omega_{nG_{r,d2}}$ are as follows:

$$\begin{cases}\xi_{G_{r,d1}}=\dfrac{K_\omega+D_\omega+K_p K_d}{2\sqrt{K_P J_\omega\omega_0}}\\ \omega_{nG_{r,d1}}=\sqrt{\dfrac{K_P}{J_\omega\omega_0}}\\ \xi_{G_{r,d2}}=\dfrac{K_\omega+D_\omega+K_p K_d}{2\sqrt{K_P\left(J_\omega\omega_0+K_d\left(K_\omega+D_\omega\right)\right)}}\\ \omega_{nG_{r,d2}}=\sqrt{\dfrac{K_P}{J_\omega\omega_0+K_d\left(K_\omega+D_\omega\right)}}\end{cases} \tag{16}$$

Comparing VSG grid-connected system with first-order virtual inertial, the relationship between the damping ratios and the natural oscillation frequencies are as follows:

$$\begin{cases}\xi_{G_{r,d1}}>\xi_{G_r}\\ \xi_{G_{r,d1}}>\xi_{G_{r,d2}}\\ \omega_{nG_{r,d1}}=\omega_{nG_r}>\omega_{nG_{r,d2}}\end{cases} \tag{17}$$

Equation (17) shows that $\xi_{G_{r,d1}}$ is always maximal, and $\xi_{G_{r,d2}}$ is greater than ξ_{G_r} within a certain range of parameter values. Therefore, VSG with improved virtual inertial can increase system damping and reduce power overshoot in the dynamic process.

D. Parameter Design

According to characteristic analysis of the VSG with improved virtual inertial based on differential compensation, $D_\omega=0$ is set to reduce the steady-state power deviation, and the system dynamic characteristics are improved by reasonable design of K_d.

When VSG operates in islanded mode, (10) and (11) are a lead-lag link, and the position of zero and pole are related to K_d. Since the inertia of the P-ω transfer function is still needed in order to keep the zero z_d and the pole s_d from constituting a pair of dipoles, the zero and the pole need to satisfy $s_d-z_d\geq-0.1s_d$. In order to avoid ignoring zero, $4s_d\leq z_d\leq s_d$ is designed. Correspondingly, K_d in (10) needs to satisfy:

$$\frac{J_\omega\omega_0}{4K_\omega}\leq K_d\leq\frac{J_\omega\omega_0}{1.1K_\omega} \tag{18}$$

K_d in (11) needs to satisfy:

$$\frac{J_\omega\omega_0}{3K_\omega}\leq K_d\leq\frac{10J_\omega\omega_0}{K_\omega} \tag{19}$$

In addition, combining the dynamic characteristic limits shown in (6)-(9), the J_ω range and K_d range of the VSG grid-connected system with improved virtual inertial based on two ways of differential compensation are shown in Fig. 9 (a) and (b), respectively.

With the same J_ω, the K_d value in Fig. 9(a) is smaller than that in Fig. 9(b). For islanded VSG, the larger K_d is, the smaller the inertia of P-ω characteristic will be, and the worse the support effect on frequency is. Therefore, the improved virtual inertial control strategy based on differential compensation at Position 1 is adopted in this paper.

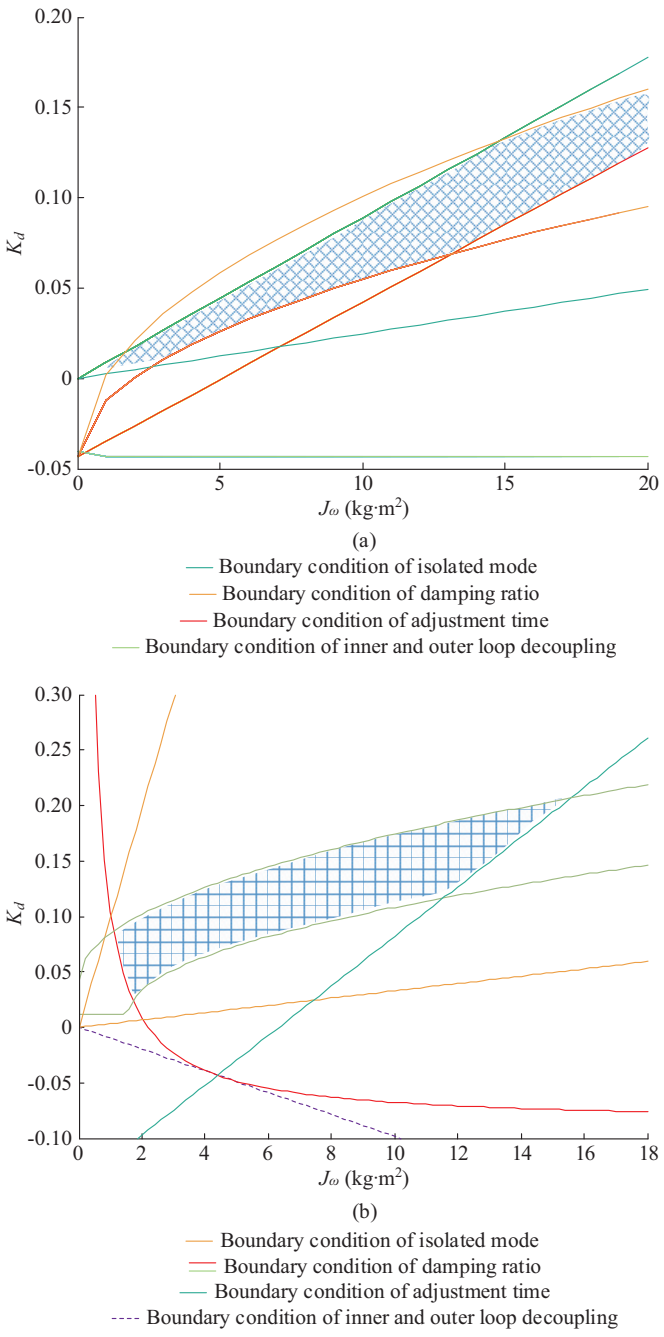

Fig. 9. J_ω and K_d range of grid-connected VSG with improved virtual inertial based on two ways of differential compensation. (a) At Position 1. (b) At Position 1.

IV. Simulation and Experimental Results

In order to verify the effectiveness of the improved virtual inertia algorithm of the VSG, a simulation platform in the MATLAB/Simulink environment and an experimental platform are built. In the simulation and experimental platforms, one VSG of 100 kW is connected to the grid. The differential term is implemented by the first-order backward difference method, and the detailed system parameters and control parameters are listed in Table I. In the experimental platforms, a TMS F2808 fixed-point digital signal processor (DSP) is adopted for the implementation of control algorithm. For the ease of data analysis and comparison, set the active power overshoot during dynamic process to be $\sigma P = (P_{\max} - P_{ref})/P_{ref}$, and the steady-state active power accuracy is $\Delta P = (P_0 - P_{ref})/P_{ref}$.

TABLE I
Parameters of Simulation and Experimental Platforms

Parameter	Value
S_{rate}	100 kW
E^*	220 V
f_s	5 kHz
C_f	90 μF
L_f	0.5 mH
U_{dc}	600 V
ω_0	314 Hz
U_g	400 V
T_f	1.6×10^{-3}
n	1.9×10^{-4} V/kvar
U_{dc}	600 V

A. Simulation Results

The VSG operates in grid-connected mode, and the grid has constant frequency, that is $\omega_g = \omega_0$. The line impedance connecting to the grid is $0.05 + j0.15\ \Omega$. At the initial time, set $P_{ref} = 0$ kW, the pre-synchronization is completed at 1.2 s, and a 50 kW step of P_{ref} occurs at 1.6 s.

Four group control strategies and control parameters of first-order virtual inertial are shown in Table II, and the corresponding output active power and angular frequency waveforms of VSG are shown in Fig. 10(a) and (b). In Fig. 10(a), when the active power reference step occurs, the output power overshoot of Group 1 is 50% in the dynamic process and cannot reach steady state until about 2.5 s later with several oscillations. In Group 2, VSG still adopts a first-order virtual inertia, while D_ω increases to K_ω for enhancing system damping ratio. The active power overshoot reduces to 12% and reaches steady state in about 2.1 s without oscillation. In Group 3, the VSG adopts a first-order virtual inertial control strategy based on differential compensation at Position 1. In dynamic process, the active power overshoot is 8%, and it reaches steady state in about 1.9 s. In Group 4, VSG adopts a first-order virtual inertial control strategy based on differential compensation at Position 2, the dynamic active power overshoot is 12%, and it reaches steady state in about 2.1 s.

Comparing the four groups of VSG output power and frequency waveforms, it can be seen that the dynamic characteristics of VSG adopting first-order virtual inertial control strategy based on differential compensation at Position 1 are the best. K_d value is the smallest, which is consistent with theoretical analysis. In Fig. 11(b), the frequency fluctuation of Group 2 is the least, and those of Group 3 and 4 are the largest. However, they are in the acceptable range compared with the inhibition effect of active power overshoot.

When VSG operates in grid-connected mode, the grid frequency deviates from its rated value, that is $\omega_g \neq \omega_0$. The oth-

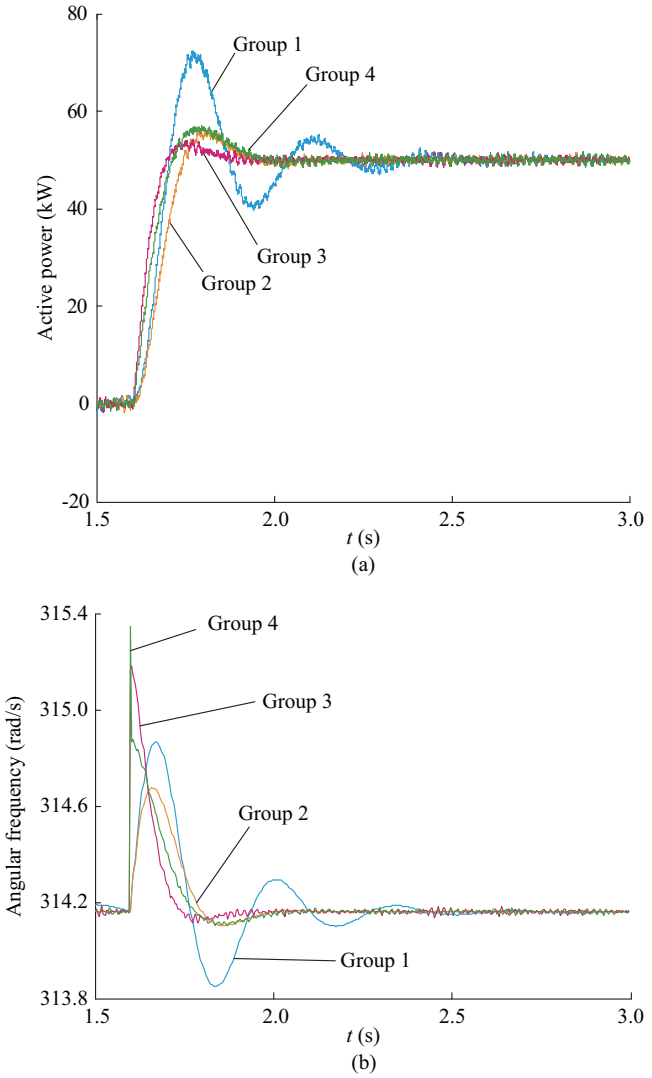

Fig. 10. Simulation waveforms of grid-connected VSG with first-order virtual algorithms (ω_g=ω_0). (a) Active power. (b) Angular frequency.

TABLE II
CONTROL STRATEGY AND CONTROL PARAMETER OF FIRST-ORDER VIRTUAL INERTIAL

Group	Control strategy	Control parameter
1	First-order virtual inertial	$J_\omega = 8, D_\omega = 0$
2	First-order virtual inertial	$J_\omega = 8, D_\omega = K_\omega$
3	Improved virtual inertial control strategy based on differential compensation at Position 1	$J_\omega = 8, D_\omega = 0$, $K_d = 0.04$
4	Improved virtual inertial control strategy based on differential compensation at Position 2	$J_\omega = 8, D_\omega = 0$, $K_d = 0.04$

er conditions are the same as that of the above simulation. The corresponding output active power and current waveforms of VSG of Group 1, Group 2 and Group 3 are shown in Fig. 11(a) and (b).

Due to $\omega_g \neq \omega_0$, there exists steady-state deviation of output active power. According to Fig. 11, with the strategy of Group 1, the steady-state power deviation is 20% and the dynamic power overshoot is 33%. In Group 2, D_ω inertially increases to K_ω, thus the dynamic power overshoot reduces to 10%, but the steady-state power deviation increases to 40%. In Group 3, with the improved virtual inertia algorithm, the dynamic power overshoot reduces to 7% and the steady-state power deviation is still 20%.

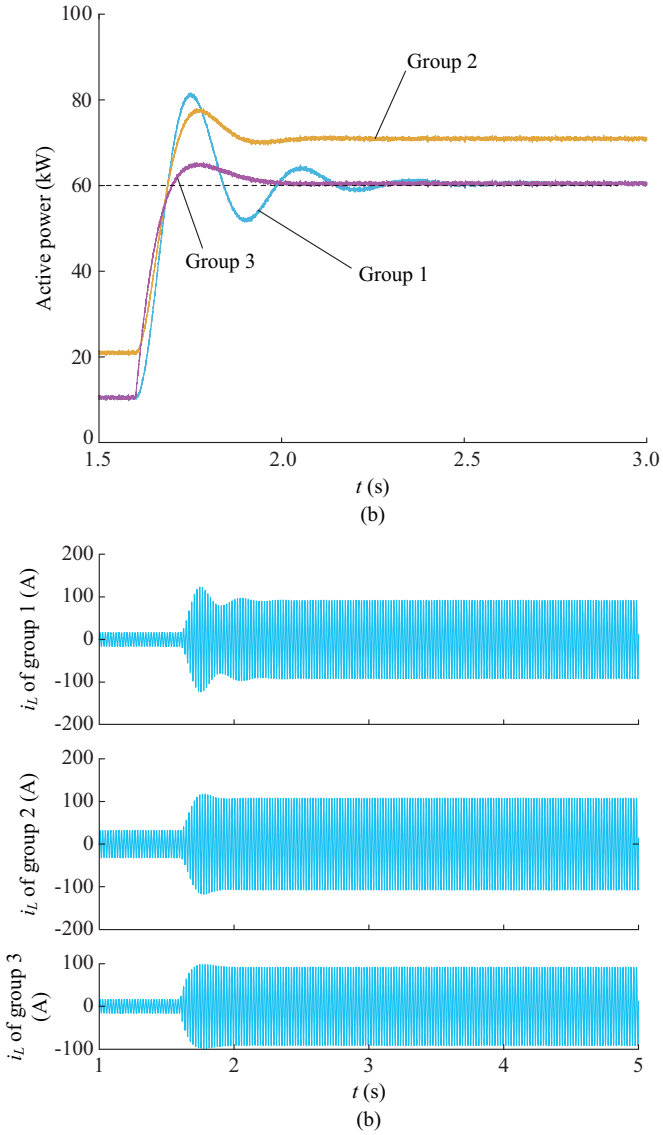

Fig. 11. Simulation waveforms of grid-connected VSG with first-order virtual inertia algorithms ($\omega_g \neq \omega_0$). (a) Output active power waveforms. (b) Current waveforms.

The simulation results are consistent with the theoretical analysis, which proves that the improved virtual inertia control strategy can reduce dynamic power impact and improve system dynamic characteristics while maintaining steady-state active power deviation.

B. Experimental Results

The experimental platform includes a VSG, a three-phase grid and a distribution cabinet. The grid is a weak grid with high penetration of DG. Its frequency fluctuates in seconds near the rated value, which leads to low-frequency fluctuation of output active power of VSG, and the fluctuation

amount is proportional to $K_\omega + D_\omega$.

VSG adopts first-order virtual inertia. Set P_{ref} = 20 kW, $K_\omega = S_{rate}/0.05\omega_0$. Figure 12 shows the waveforms of output voltage angular frequency of VSG, active power, and output current with active power reference stepping from 20 kW to 40 kW. In Fig. 12(a), J_ω = 8, D_ω = 0; in Fig. 12(b), J_ω = 8, $D_\omega = K_\omega$.

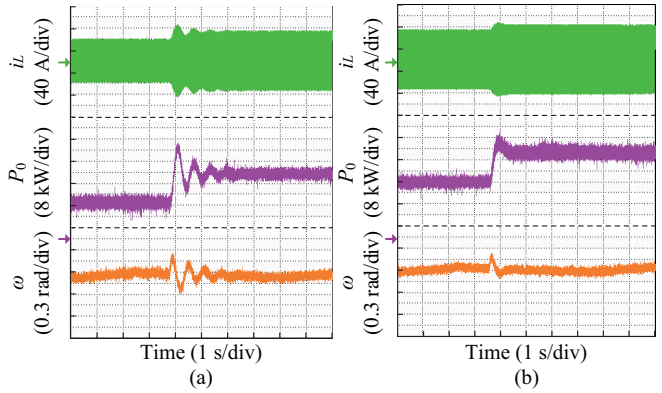

Fig. 12. Experiment waveforms of grid-connected VSG with first-order virtual inertia. (a) J_ω = 8, D_ω = 0. (b) J_ω = 8, $D_\omega = K_\omega$.

In Fig. 12(a), due to a large value of J_ω, when active power reference steps, the VSG output power oscillates and restores to steady state in 2.6 s, and the power overshoot is 40% in dynamic process. In steady state, owing to $\omega_0 \neq \omega_g$, the VSG output power is 8 kW larger than the reference value. It illustrates that the increase of J_ω reduces system stability and increases the power impact of energy storage unit. In order to improve the dynamic performance of active power, in Fig. 12(b), D_ω increases. Thus, the system damping ratio increases, and the power overshoot decreases to 20%. However, the steady-state deviation of active power increases to 16 kW simultaneously. Therefore, when VSG with first-order virtual inertial strategy operates in grid-connected mode, there is a contradiction between steady-state and dynamic characteristics of output active power.

When the active power reference steps from 20 kW to 40 kW, Fig. 13 shows the output voltage angular frequency, active power, and output current waveforms of VSG, which adopts improved virtual inertial algorithm based on differential compensation at Position 1, and J_ω = 8, K_d = 0.04.

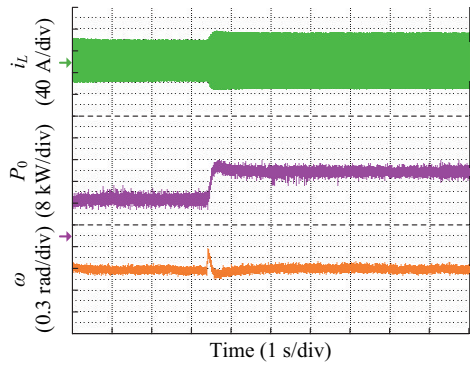

Fig. 13. Experiment waveforms of grid-connected VSG with improved virtual inertia algorithm based on differential compensation at Position 1.

The differential compensation link increases system damping and accelerates response speed, and power oscillation does not occur. The dynamic process is shortened to 0.6 s, and power overshoot decreases to 16%. In steady state, the active power deviation still maintains at 8 kW.

When the active power reference steps from 20 kW to 40 kW, the VSG adopts the improved virtual inertial algorithm based on differential compensation at Position 2, and J_ω = 8, K_d = 0.04. Waveforms of VSG output voltage angular frequency, active power, and output current are shown in Fig. 14.

In Fig. 14, power oscillation also does not occur, the dynamic process is shortened to 0.8 s, and power overshoot decreases to 20%. In steady state, the active power deviation still maintains at 8 kW. Therefore, in the case of the same differential coefficient, the system with improved virtual inertial control strategy based on differential compensation at Position 1 has a greater system damping ratio and faster response speed.

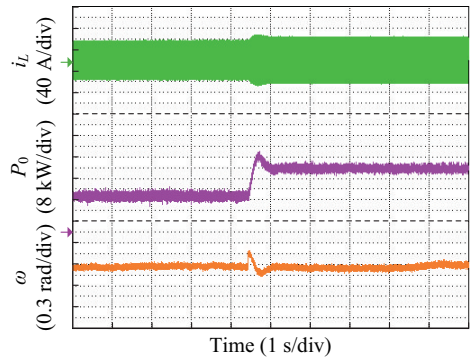

Fig. 14. Experiment waveforms of grid-connected VSG with improved virtual inertia based on differential compensation at Position 2.

The experimental result comparison of VSG with different virtual inertial algorithms is given in Table III.

TABLE III
EXPERIMENTAL RESULT COMPARISON OF VSG WITH DIFFERENT IMPROVED VIRTUAL INERTIAL ALGORITHMS

Control strategy	Parameters	Experimental results
First-order virtual inertial	J_ω = 8, D_ω = 0	σP = 40%, ΔP = 8 kW
First-order virtual inertial	J_ω = 8, $D_\omega = K_\omega$	σ_P = 20%, ΔP = 16 kW
Improved virtual inertial control strategy based on differential compensation at Position 1	J_ω = 8, D_ω = 0, K_d = 0.04	σP = 16%, ΔP = 8 kW
Improved virtual inertial control strategy based on differential compensation at Position 2	J_ω = 8, D_ω = 0, K_d = 0.04	σ_P = 20%, ΔP = 8 kW

V. CONCLUSION

In order to eliminate the regulation contradiction between steady-state deviation of output active power and dynamic impact of VSG operating in grid-connected mode, an improved virtual inertia algorithm is proposed. By setting D_ω = 0, the coupling effect of D_ω on active power steady-state deviation and dynamic characteristics is eliminated, and the

steady-state power deviation is maintained. Furthermore, two forms of improved virtual inertia algorithms are put forward by cascading a differential link into different positions of first-order virtual inertia forwarding channel to replace the regulation effect of D_ω on active power dynamic features, so as to reduce dynamic power impact. Then, by theoretical analysis, the improved virtual inertial strategy based on differential compensation at Position 1 is proved to have better dynamic features. With the improved virtual inertia algorithm, the dynamic power characteristic is improved and its steady-state characteristic is maintained. Simulation and experimental results show that VSG with the existing first-order virtual inertia strategy reduces dynamic power impact. However, the steady-state power deviation is increased simultaneously, while the VSG with the improved virtual inertia strategy can reduce dynamic power impact and maintain steady-state power deviation. Future work will focus on exploring more varied forms of improved virtual inertia, summarizing the improvement rules, and studying the characteristics of the system with several VSGs.

REFERENCES

[1] W. D. Xiao, F. F. Edwin, G. Spagnuolo *et al*., "Efficient approaches for modeling and simulating photovoltaic power systems," *IEEE Journal of Photovoltaics*, vol. 3, no. 1, pp. 500-508, Jan. 2013.

[2] X. Ye, J. Le, Y. Y. Liu *et al*., "A coordinated consistency voltage stability control method of active distribution grid," *Journal of Modern Power Systems and Clean Energy*, vol. 6, no. 1, pp. 85-94, Jan. 2018.

[3] C. Yu, X. Zhang, F. Liu *et al*., "Modeling and resonance analysis of multi-parallel inverters system under asynchronous carriers conditions," *IEEE Transactions on Power Electronics*, vol. 32, no. 4, pp. 3192-3205, Apr. 2017.

[4] S. Bahrami and F. Safe, "A financial approach to evaluate an optimized combined cooling, heat and power system," *Energy and Power Engineering*, vol. 5, no. 5, pp. 352-362, Jan. 2013.

[5] M. H. Amini, K. G. Boroojeni, T. Dragičević *et al*., "A comprehensive cloud-based real-time simulation framework for oblivious power routing in clusters of DC microgrids," in *Proceedings of 2017 IEEE Second International Conference on DC Microgrids*, Nuremburg, Germany, Jun. 2017, pp. 270-273.

[6] C. Konstantopoulos and E. Koutroulis, "Global maximum power point tracking of flexible photovoltaic modules," *IEEE Transactions on Power Electronics,* vol. 29, no. 6, pp. 2817-2828, Jun. 2014.

[7] H. P. Beck and R. Hesse, "Virtual synchronous machine," in *Proceedings of 2007 9th International Conference on Electrical Power Quality and Utilisation*, Barcelona, Spain, Nov. 2007, pp. 1-6.

[8] Q. C. Zhong and G. Weiss, "Synchronverters: inverters that mimic synchronous generators," *IEEE Transactions on Industrial Electronics*, vol. 58, no. 4, pp. 1259-1267, May 2011.

[9] F. Gao and M. R. Iravani, "A control strategy for a distributed generation unit in grid-connected and autonomous modes of operation," *IEEE Transactions on Power Delivery*, vol. 23, no. 2, pp. 850-859, Jun. 2008.

[10] Q. C. Zhong, "Virtual synchronous machines: a unified interface for grid integration," *IEEE Power Electronics Magazine*, vol. 3, no. 4, pp. 18-27, Dec. 2016.

[11] X. D. Liang and C. A. B. Karim, "Virtual synchronous machine method in renewable energy integration," in *Proceedings of 2016 IEEE PES Asia-Pacific Power and Energy Engineering Conference (APPEEC)*, Xi'an, China, Oct. 2016, pp. 1-5.

[12] J. Meng, Y. Wang, C. Fu *et al*., "Adaptive virtual inertia control of distributed generator for dynamic frequency support in microgrid," in *Proceedings of 2016 IEEE Energy Conversion Congress and Exposition*, Milwaukee, USA, Sept. 2016, pp. 1-5.

[13] J. Alipoor, Y. Miura, and T. Ise, "Power system stabilization using virtual synchronous generator with alternating moment of inertia," *IEEE Journal of Emerging and Selected Topics in Power Electronics*, vol. 3, no. 2, pp. 451-458, Jun. 2015.

[14] J. Alipoor, Y. Miura, and T. Ise, "Distributed generation grid integration using virtual synchronous generator with adoptive virtual inertia," in *Proceedings of 2013 IEEE Energy Conversion Congress and Exposition*, Denver, USA, Sept. 2013, pp. 4546-4552.

[15] R. L. Shi, X. Zhang, C. Hu *et al*., "Self-tuning virtual synchronous generator control for improving frequency stability in autonomous photovoltaic-diesel microgrids," *Journal of Modern Power Systems and Clean Energy*, vol. 6, no. 3, pp. 482-494, Dec. 2018.

[16] M. A. Torres, L. A. C. Lopes, L. A. Morán *et al*., "Self-tuning virtual synchronous machine: a control strategy for energy storage systems to support dynamic frequency control," *IEEE Transactions on Energy Conversion*, vol. 29, no. 4, pp. 833-840, Dec. 2014.

[17] N. Soni, S. Doolla, and M. C. Chandorkar, "Inertia design methods for islanded microgrids having static and rotating energy sources," *IEEE Transactions on Industry Applications*, vol. 52, no. 6, pp. 5165-5174, Nov. 2016.

[18] Y. Du, J. M. Guerrero, L. Chang *et al*., "Modeling, analysis, and design of a frequency-droop-based virtual synchronous generator for microgrid applications," in *Proceedings of 2013 IEEE ECCE Asia Downunder*, Melbourne, Australia, Jun. 2013, pp. 643-649.

[19] J. He, Y. W. Li, J. M. Guerrero *et al*., "An islanding microgrid power sharing approach using enhanced virtual impedance control scheme," *IEEE Transactions on Power Electronics*, vol. 28, no. 11, pp. 5272-5282, Nov. 2013.

[20] M. P. N. van Wesenbeeck, S. W. H. de Haan, P. Varela *et al*., "Grid tied converter with virtual kinetic storage," in *Proceedings of 2009 IEEE Bucharest PowerTech*, Bucharest, Romania, Aug. 2009, pp. 1-7.

[21] R. Aouini, K. Ben Kilani, B. Marinescu *et al*., "Virtual synchronous generators dynamic performances," in *Proceedings of 2014 International Conference on Electrical Sciences and Technologies in Maghreb*, Tunis, Tunisia, Nov. 2014, pp. 1-6.

[22] B. S. Chen, *Control Systems of Electric Drives-motion Control Systems*, Beijing, China: China Machine Press, 2006.

[23] H. Alatrash, A. Mensah, E. Mark *et al*., "Generator emulation controls for photovoltaic inverters," *IEEE Transactions on Smart Grid*, vol. 3, no. 2, pp. 996-1011, Oct. 2012.

[24] H. Z. Xu, X. Zhang, F. Liu *et al*., "Virtual synchronous generator control strategy based on differential compensation virtual inertia," *Automation of Electric Power Systems*, vol. 41, no. 3, pp. 96-102, Apr. 2017.

Haizhen Xu received the B.S. and Ph.D. degrees from the College of Electrical Engineering and Automation from Hefei University of Technology, Hefei, China, in 2010 and 2017, respectively. She has been a faculty member of the Department of Electronic Information and Electrical Engineering, Hefei University, Hefei, China. Her current research interests include control of VSG converters, parallel converter systems, and photovoltaic generation technologies.

Changzhou Yu received the B.S. and Ph.D. degrees in Electrical Engineering and Automation from Hefei University of Technology, Hefei, China, in 2009 and 2016. Since 2017, he has been a faculty member of the Department of Electronic Information and Electrical Engineering, Hefei University. His current research interests include control of photovoltaic converters, parallel converter systems, and distributed generation systems.

Chun Liu received the B.S. degree in automation and the M.S. and Ph.D. degrees in electrical engineering from Hefei University of Technology, Hefei, China, in 2004, 2008, and 2016, respectively. Since 2017, he has been a faculty member of the Department of Electronic and Electrical Engineering, Hefei University, Hefei, China. His current research interests include wind power generation technologies, and distributed generation systems.

Qinglong Wang received the B.S. and M.S. degrees from Anhui University of Science and Technology, China, and the Ph.D. degree in electrical engineering and automation from Hefei University of Technology, China, in 1996, 2004, and 2007, respectively. He joined the Department of Electronics and Electrical Engineering, Hefei University, China, in 2007, where he is currently a Professor. His research and teaching interests include dynamic modeling and optimized design of electrical machines, wind power generation technologies, and distributed generation system.

Xing Zhang received the B.S., M.S. and Ph.D. degrees in electrical engineering and automation from Hefei University of Technology, Hefei, China, in1984, 1990, and 2003, respectively. Since 1984, he has been a faculty member of the School of Electrical Engineering and Automation, Hefei University of Technology, where he is currently a Professor and is also with the Photovoltaic Engineering Research Center of Ministry of Education. His main research interests include photovoltaic generation technologies, wind power generation technologies, and distributed generation system.